



**HAL**  
open science

## A sparsity-based variational approach for the restoration of SMOS images from L1A data

Javier Preciozzi, Andrès Almansa, Pablo Musé, Sylvain Durand, Ali Khazaal, Bernard Rougé

### ► To cite this version:

Javier Preciozzi, Andrès Almansa, Pablo Musé, Sylvain Durand, Ali Khazaal, et al.. A sparsity-based variational approach for the restoration of SMOS images from L1A data. 2016. hal-01341839v1

**HAL Id: hal-01341839**

**<https://hal.science/hal-01341839v1>**

Preprint submitted on 5 Jul 2016 (v1), last revised 20 Mar 2017 (v2)

**HAL** is a multi-disciplinary open access archive for the deposit and dissemination of scientific research documents, whether they are published or not. The documents may come from teaching and research institutions in France or abroad, or from public or private research centers.

L'archive ouverte pluridisciplinaire **HAL**, est destinée au dépôt et à la diffusion de documents scientifiques de niveau recherche, publiés ou non, émanant des établissements d'enseignement et de recherche français ou étrangers, des laboratoires publics ou privés.

# A sparsity-based variational approach for the restoration of SMOS images from L1A data

Javier Preciozzi, Andrés Almansa, Pablo Musé, Sylvain Durand, Ali Khazaal and Bernard Rougé

**Abstract**—The SMOS mission senses ocean salinity and soil moisture by measuring Earth’s brightness temperature using interferometry in the L-band. These interferometry measurements known as *visibilities* constitute the SMOS L1A data product. Despite the L-band being reserved for Earth observation, the presence of illegal emitters cause radio frequency interference (RFI) that mask the energy radiated from the Earth and strongly corrupt the acquired images. Therefore, the recovery of brightness temperature from corrupted data by image restoration techniques is of major interest. In this work we propose a variational model to recover super-resolved, denoised brightness temperature maps by decomposing the images into two components: an image  $T$  that models the Earth’s brightness temperature and an image  $O$  modeling the RFIs. Experiments with synthetic and real data support the suitability of the proposed approach.

**Index Terms**—SMOS, MIRAS, RFI, brightness temperature, non-differentiable convex optimization, total variation minimization.

## I. INTRODUCTION

Observing Earth variables such as surface soil moisture (SSM) and sea surface salinity (SSS) is crucial to obtain meteorological and climate predictions [1]. The SMOS satellite [2] carries an instrument called MIRAS (Microwave Imaging Radiometer by Aperture Synthesis) [3], [4], that provides indirect measurements of the corresponding brightness temperatures of both SSM and SSS in the L-band microwave, using interferometry.

### A. From brightness temperatures to visibilities: The MIRAS instrument and the forward problem

The interferometry principle used by the MIRAS instrument [3], [4] can be formalized by means of the *visibility function* [5], that relates brightness temperatures with visibilities. The antennas configuration chosen for MIRAS instrument is a Y-shaped array, where each arm is composed by a set of regularly spaced passive antennas (see Figure 1, left figure). Let  $(A_k, A_l)$  be any pair of its antennas; the visibility function

$V(\mathbf{u}_{kl})$  is defined as the complex cross-correlation between the received signals at  $A_k$  and  $A_l$ :

$$V(\mathbf{u}_{kl}) = \frac{1}{\sqrt{\Omega_k \Omega_l}} \iint_{\|\boldsymbol{\xi}\| \leq 1} U_k(\boldsymbol{\xi}) U_l^*(\boldsymbol{\xi}) (T_b(\boldsymbol{\xi}) - T_r) \tilde{r}_{kl}(t) \frac{e^{-i2\pi \mathbf{u}_{kl}^T \boldsymbol{\xi}} d\boldsymbol{\xi}}{\sqrt{1 - \|\boldsymbol{\xi}\|^2}}. \quad (1)$$

Here  $U_k$  and  $U_l$  are the corresponding normalized voltage patterns of the antennas;  $\Omega_k, \Omega_l$  their corresponding solid angles;  $\mathbf{u}_{k,l} = (u_1^{kl}, u_2^{kl})$  is the spacing between the two antennas  $(A_k, A_l)$  in wavelength. The Cartesian coordinates  $\boldsymbol{\xi} = (\xi_1, \xi_2)$  are the spatial domain coordinates, which are restricted to the unit circle.  $T_r$  is the physical temperature of the receivers (assumed the same for all receivers);  $\tilde{r}_{kl}$  is the Fringe-Wash function, a function of the spatial delay  $t = \frac{\mathbf{u}_{kl}^T \boldsymbol{\xi}}{f_0}$ , where  $f_0 = \frac{c}{\lambda_0}$  is the central frequency of observation. Note that the brightness temperature  $T_b$  is a 2D function defined on the unit circle  $\{\boldsymbol{\xi} : \|\boldsymbol{\xi}\| \leq 1\}$  [5], [6].

Since the brightness temperature support is the unit circle, it is well known that the best regular sampling grid is a hexagonal one [7], leading to the largest alias-free Field of View for a given spacing between the antennas [8]. The antennas configuration chosen for the MIRAS instrument is a Y-shaped array [8], shown in Figure 1 along with its corresponding hexagonally sampled, star-shaped domain  $H$ . This star-shaped domain  $H$ , known in aperture synthesis as the *experimental frequency coverage* [9, Ch. 5], is contained within the hexagon, hence requiring extrapolation to recover the missing parts (see Figure 2). Because of other practical

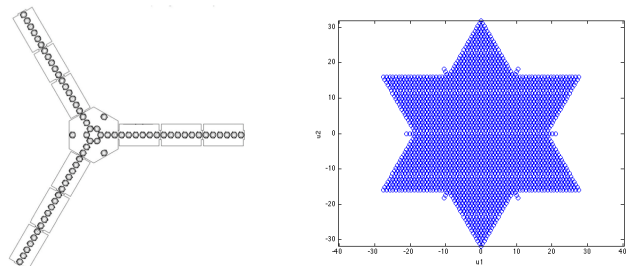


Fig. 1. Diagram of the MIRAS instrument onboard of SMOS satellite (from [10]) and the star-shaped, hexagonally sampled visibilities domain derived from it. The number of antennas in the miras instrument is 69: 22 antennas type Light-Weight Cost-Effective Front-End (LICEF) in each arm, plus three antennas of type Noise Level Injection Radiometers (NIR) located in-between each arm in the center of the instrument.

Javier Preciozzi and Pablo Musé are with the Department of Electrical Engineering, Facultad de Ingeniería, Universidad de la República, Uruguay.

Andrés Almansa is with LTCI - Télécom ParisTech, France.

Sylvain Durand is with MAP5, Université René Descartes, France.

Ali Khazaal and Bernard Rougé are with the Centre d’Etudes Spatiales de la Biosphère (CESBIO), France.

This work has been partially funded by the French Research Agency (ANR) under grant nro ANR-14-CE27-0019 (MIRIAM).

issues, the final separation between antennas in the MIRAS instrument is  $d := \|\mathbf{u}_{kl}\| = 0.875$  wavelengths, for any

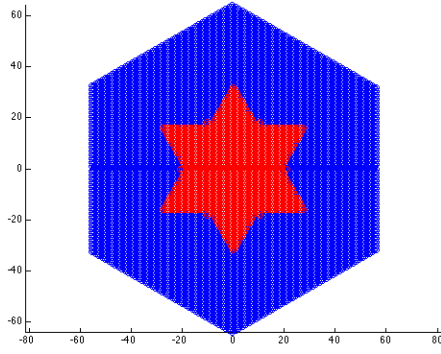
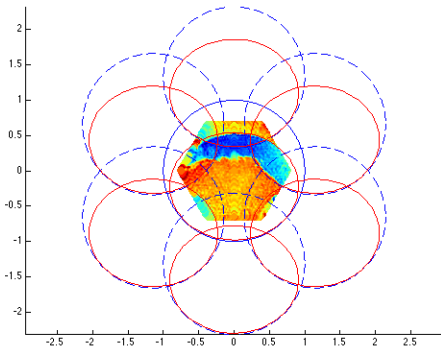


Fig. 2. The absence of information beyond the *experimental frequency coverage*  $H$  (in red) makes the recovery of the brightness temperature map an ill-posed problem.

$k \neq l$  within each arm. This value is larger than the critical sampling distance on a hexagonal grid (which is  $d = 1/\sqrt{3}$  wavelengths), and then, some aliasing is introduced on the spatial domain. Figure 3 shows the spatial domain and its six replicas, where the Alias-Free Field of View is the small central zone in the hexagon delimited by the blue dashed lines. Because of the tilt of the satellite acquisition system, most of the aliasing comes from the intersection between the Earth disk with the known cold sky (whose values are known) and therefore it is customary to consider the Field of View delimited by the red plain lines: the *Extended Alias-Free Field of View* (E-AF-FOV) [8].



Normalized spatial domain ( $\xi_1, \xi_2$ )

Fig. 3. Alias Free - Field of View (AF-FOV) – zone delimited by the unity circle contours in blue lines – and the corresponding Extended Alias-Free Field of View (E-AF-FOV) in red lines. See text for details.

### B. Restoring brightness temperatures from visibilities: An ill-posed inverse problem

Going back to Equation (1), if we define  $T = T_b - T_r$ , the samples of  $T$  in the hexagonal grid can be obtained from the visibility samples by solving the linear system  $\mathbf{G}T = V$ , where matrix  $\mathbf{G}$  represents the discrete linear operator given by (1). Of course, the inversion of this problem is ill-posed since  $\mathbf{G}$  is not invertible. The ill-posedness of the problem

can also be interpreted as a lack of information beyond  $H$ , as illustrated in Figure 2. Hence, additional constraints must be added to the model. In [6], the authors propose to solve it as a constrained least square minimization problem, imposing that  $T$  has no frequency components outside  $H$ . This problem can be formulated as an unconstrained minimisation:

$$\hat{T}_{sol} = \min_{\hat{T}} \|V - \mathbf{G}\mathbf{F}^*\mathbf{Z}_H\hat{T}\|_2^2 \quad (2)$$

where  $\mathbf{F}^*$  denotes the matrix corresponding to the hexagonal Inverse Fourier Transform,  $\mathbf{Z}_H$  the zero padding operator beyond  $H$  and  $\hat{T}$  the Fourier coefficients of  $T$  for frequencies in  $H$ . This minimisation problem has a direct solution:  $\hat{T} = \mathbf{J}^+V$  where  $\mathbf{J} = \mathbf{G}\mathbf{F}^*\mathbf{Z}_H$  and  $\mathbf{J}^+ = (\mathbf{J}^*\mathbf{J})^{-1}\mathbf{J}^*$  is the pseudo-inverse of  $\mathbf{J}$ . Finally,  $T$  can be obtained from  $\hat{T}$  very easily applying an inverse Fourier transform. This approach is the nominal image reconstruction process of the SMOS pipeline and corresponds exactly to the L1B product. It is well known that a zero padding on the Fourier domain may lead to Gibbs effects on the restored image. This can be partially alleviated (as proposed by [6]) by the use of a Blackman window  $\mathbf{B}$ :  $T = \mathbf{F}^*\mathbf{B}\mathbf{Z}_\Omega\hat{T}$ .

This approach (that we will refer in what follows as the *zero padding* approach), has many advantages: it has a clear physical interpretation (values outside  $H$  are set to zero), it is very fast (since only a matrix multiplication is needed to obtain  $\hat{T}$ ), and in general gives good results. Nevertheless, this is not the case when the visibilities are corrupted by radio frequency interferences (RFI). Because these RFIs have frequencies beyond  $H$  and their power is far stronger than Earth radiation, very strong Gibbs effects can be seen on the final *brightness temperature* images (see for instance the top left image in Figure 10 corresponding to western Europe, obtained by the nominal reconstruction process [6]).

### C. Proposed approach and contributions

In this work we propose a novel formulation to solve the inverse problem presented on (1) using a variational formulation that explicitly models the formation of visibilities as a superposition of the Earth's natural brightness temperatures and the RFIs. As it will be demonstrated later, the proposed approach automatically removes signal effects generated from RFIs, while at the same time extrapolates the image spectrum in order to minimize Gibbs effects, with no *a priori* knowledge of the RFIs locations. A preliminary, short version of this work was presented in IGARSS 2014 [11].

The article is organized as follows. In Section II we present the model on which our restoration approach is based, and we explain how this model can be solved using state of the art optimization techniques. In Section III we describe in detail numerical issues to make the problem numerically tractable. The definitive implementation is presented in Section IV, where we discuss major issues like parameter choices and numerical optimization. In Section V we present experiments with synthetic data that validate the proposed approach and we also apply our method to real L1A SMOS data and we

compare them with results obtained using the *zero padding* and the *Blackman* approach. For the sake of brevity, a large set of experiments is presented in the complementary material. Conclusions and future work are presented in Section VI.

## II. MODELIZATION AND VARIATIONAL FORMULATION: A FIRST APPROXIMATION TO THE PROBLEM

Visibilities and *brightness temperatures* are related by the linear operator given by (1). In its discrete form, using matrix notation<sup>1</sup>, this is  $\mathbf{G}T = V$ . As before, the goal is to obtain the original temperatures image  $T$  from the given visibilities  $V$ , knowing that, as noted before,  $\mathbf{G}$  is not invertible. We propose to model the observed brightness temperature image  $\tilde{T}$  as

$$\tilde{T} = T + O, \quad (3)$$

where  $T$  is the non-polluted Earth's *brightness temperature* image and  $O$  is the outliers' image generated by the RFIs that are assumed to be sparse pointwise sources (delta functions). Because of the physical acquisition system, the visibilities are corrupted with noise, that under realistic assumptions can be considered to be a Gaussian white noise with 0 mean and standard deviation  $\sigma_{\Delta V_L}$  [12]. The final equation is then:

$$\mathbf{G}\tilde{T} + n = \mathbf{G}(T + O) + n = V \quad (4)$$

where  $V$  is the vector of measured visibilities which are corrupted by the additive Gaussian noise  $n$  described before.

### A. Variational formulation

We propose to recover  $T$  by solving the following constrained minimization problem:

$$(T_{sol}, O_{sol}) = \min_{T, O} \{TV(T) + \mu S(O)\} \quad (5)$$

such that  $\|\mathbf{G}(T + O) - V\|_2^2 \leq |H|\sigma_{\Delta V_L}^2$ ,

In this formulation,  $TV(\cdot)$  denotes the total variation seminorm (Appendix A) and  $S(\cdot)$  is a norm that promotes sparsity of the outliers image  $O_{sol}$ , for instance the  $\ell_1$  norm or the  $\ell_0$  counting measure (Appendix A). Parameter  $\mu$  controls the trade-off between both terms; its choice can be formally derived from geometric considerations on the outliers, and will be discussed in detail in Section IV-A2. The data fit term is derived directly from the white, Gaussian distributed data noise model  $n = \mathbf{G}(T + O) - V$ . The bound  $|H|\sigma_{\Delta V_L}^2$  represents the area of  $H$  times the visibilities variance  $\sigma_{\Delta V_L}^2$ . It is well known that the minimization of the  $\ell_2$  norm corresponds to the *Maximum A Posteriori* estimator of white Gaussian noise.

**Remark:** The total variation is used to super-resolve  $T$  beyond the *experimental frequency coverage*  $H$  while avoiding Gibbs oscillations: it is a complete substitution for the *zero padding* approach, where instead of filling the coefficients outside  $H$  with zero, they are recovered by the  $TV$  minimization [13]. In the other hand, the sparsity operator is chosen to model the RFIs image  $O$  since this image is zero almost everywhere because RFIs are very sparse. It

is well known that  $\ell_1$  or  $\ell_0$  norm promotes sparsity [14]: image  $O_{sol}$  will be a sparse image composed by only the RFIs.

Problem (5) can be reformulated as an unconstrained one:

$$(T_{sol}, O_{sol}) = \min_{T, O} \|\mathbf{G}(T + O) - V\|_2^2 + \lambda(TV(T) + \mu S(O)), \quad (6)$$

where the Lagrange multiplier  $\lambda$  must be chosen to ensure equivalence between both problems. The derivation of  $\lambda$  is addressed in Section IV-A.

When  $S(\cdot)$  is the  $\ell_1$  norm, problem (6) is convex, and despite not being strictly convex, it has a unique local minimum ([15], [16]). However, a careful treatment has to be taken since the term multiplied by  $\lambda$  is non-differentiable. Fortunately, there exist optimization methods to solve this kind of problems. One of them is the *Forward-Backward* (FB) splitting algorithm [17], while other splitting approaches such as the Split-Bregman method could also be used<sup>2</sup>:

**Proposition 1.** *Let  $E(x) = E_1(x) + E_2(x)$ , where  $E_1$  and  $E_2$  are convex functions such that  $E_1$  is differentiable with Lipschitz gradient, and  $E_2$  is a simple function, in the sense that its associated proximal operator*

$$\text{prox}_{\gamma E_2}(x) = \arg \inf_y E_2(y) + \frac{1}{2\gamma} \|x - y\|^2 \quad (7)$$

*admits a closed form or a simple algorithm to compute it. If these hypotheses hold, the following generic algorithm can be derived: for each  $k \in \mathbb{N}$ , the  $k$ -th iteration starting from seed  $x^0 = (T^0, O^0)$  is given by*

$$\begin{cases} x^{k+1/2} &= x^k - \gamma \nabla E_1(x^k) \\ x^{k+1} &= \text{prox}_{\gamma E_2}(x^{k+1/2}). \end{cases}$$

*In order to ensure convergence to the minimizer,  $\gamma$  must be smaller than  $2/L$ , where  $L$  is the Lipschitz constant of  $\nabla E_1$ .*

In our case, we have  $E_1(T, O) = \|\mathbf{G}(T + O) - V\|_2^2$  and  $E_2(T, O) = \lambda(TV(T) + \mu S(O))$  that yields

$$\begin{aligned} \nabla E_1(T, O) &= \begin{pmatrix} \mathbf{G}^* \mathbf{G}(T + O) - V \\ \mathbf{G}^* \mathbf{G}(T + O) - V \end{pmatrix}, \\ \text{prox}_{\gamma E_2}(T, O) &= \begin{pmatrix} \text{prox}_{\gamma \lambda TV}(T) \\ \text{prox}_{\gamma \lambda \mu \|\cdot\|_1}(O) \end{pmatrix}. \end{aligned}$$

It is straightforward to show from (7) that the  $\text{prox}_{\gamma \lambda \mu \|\cdot\|_1}(O)$  corresponds to the *soft thresholding* operator (see Appendix A):

$$s_{\Delta}(t) = \begin{cases} \text{sign}(t)(|t| - \Delta) & \text{if } |t| \geq \Delta, \\ 0 & \text{if } |t| < \Delta. \end{cases}$$

Although  $\text{prox}_{\gamma \lambda TV}(T)$  has not an explicit form, there exist several algorithms that solve this proximal operator ([15], [16]). In Appendix A we explain the one used in this work. The algorithm described so far converges to the unique global minimizer that corresponds to the solution of problem (5) with sparsity operator  $S(O) = \|O\|_1$ . We use this solution as an initialisation for the second step, where the sparsity operator

<sup>2</sup>We decide to use FB since, while the parameters in FB follow naturally from the implementation, whereas parameters involved in the SB algorithm are related to convergence rate and are therefore harder to set.

<sup>1</sup>For the sake of simplicity, we use the same notation to refer to an image and its vectorized form. Disambiguation follows easily from the context.

is chosen to be  $S(O) = \|O\|_0$ , which is non-convex. For this problem, the same FB algorithm can be considered and is guaranteed to converge to a local minimizer [18]. Now, instead of the soft thresholding, the proximal operator for  $S(O) = \|O\|_0$  becomes the hard thresholding  $h_{\sqrt{2\gamma\lambda\mu}}(t) = t \mathbb{1}_{\{|t| \geq \sqrt{2\gamma\lambda\mu}\}}$  (see appendix A). The reason to run the FB algorithm with  $\|O\|_0$  is to exploit even more the sparsity characteristics of the problem, since it is known that norm  $\|O\|_0$  leads to a sparser solution than  $\|O\|_1$  [14].

### III. NUMERICAL ISSUES

#### A. Matrix $\mathbf{G}^*\mathbf{G}$

The FB algorithm requires a multiplication by matrix  $\mathbf{G}^*\mathbf{G}$  at each iteration. Matrix  $\mathbf{G}$  is a  $4695 \times 16384$  matrix: 4695 is the number of visibilities and 16384 is the number of samples of the *brightness temperature*. It follows that matrix  $\mathbf{G}^*\mathbf{G}$  is  $16384 \times 16384$ . Because it is a dense matrix, a great number of operations are performed at each iteration, which is computationally not desirable. However, a change of basis to the Fourier domain yields:

$$\nabla E_1(T, O) = \mathbf{F}^*((\mathbf{GF}^*)^*\mathbf{GF}^*\mathbf{F}(T+O) - (\mathbf{GF}^*)^*V), \quad (8)$$

where  $\mathbf{F}$  is the matrix representation of the Fourier transform (and  $\mathbf{F}^*$  its conjugate). The advantage of this representation is that matrix  $((\mathbf{GF}^*)^*\mathbf{GF}^*$  reveals a highly sparse structure: to keep the Frobenius norm of  $((\mathbf{GF}^*)^*\mathbf{GF}^*$  at 99.99% of its value, we only need to keep 0.0008 of its entries. From a computational point of view, solving Equation 8 can be done even more efficiently using a standard Fast Fourier Transform implementation:

$$\nabla E_1(T, O) = \mathcal{F}^*((\mathbf{GF}^*)^*\mathbf{GF}^*\mathcal{F}(T+O) - (\mathbf{GF}^*)^*V), \quad (9)$$

where  $\mathcal{F}$  denotes the Cooley and Tuckey standard Fast Fourier Transform, that we use instead of matrix multiplication by the matrix  $\mathbf{F}$ .

The property of being sparse on the Fourier domain can be easily understood from the image formation point of view: each of the visibilities values corresponds to the cross-correlation of two signals received at two different antennas. Clearly, if the antennas are close to each other this correlation is high, but the farther they get it tends to be negligible.

The use of the standard (rectangular) FFT on a hexagonal lattice can be made possible by re-projecting the samples in a rectangular grid (see [8] or [19, Section III]). Consequently, we can modify the FB algorithm described above to perform the minimization in the Fourier domain. This implementation is summarized in Algorithm 1 (where all the variables have the same meaning as before).

#### B. Spectral TV

In order to reduce the ‘‘staircasing’’ effect inherent to many TV minimization methods( [20], [21]), we use an approach inspired on the *Spectral TV* method proposed by Moisan [22]. In Moisan’s approach, staircasing reduction is achieved by: (i) Computing image derivatives not by finite differences but analytically on the Fourier series expansion; (ii) Approximating

#### Proposed method with Forward-Backward implementation

**input :** A vector of visibilities  $V$

**output:** A brightness temperature image  $T$ , and an RFIs image  $O$

**initialization:**

**Step 0:**

- Set  $T^0 = 0$  and  $O^0 = 0$
- Choose  $\gamma < 2/L$ , where  $L$  is the Lipschitz constant of  $\nabla(E_1)$

**Step k ( $k \geq 0$ ):**

$$\begin{cases} T^{k+1/2} &= T^k - \gamma \mathcal{F}^*(\mathbf{FG}^*\mathbf{GF}^*\mathcal{F}(T^k + O^k) - \mathbf{FG}^*)V \\ O^{k+1/2} &= O^k - \gamma \mathcal{F}^*(\mathbf{FG}^*\mathbf{GF}^*\mathcal{F}(T^k + O^k) - \mathbf{FG}^*)V \\ T^{k+1} &= \text{prox}_{\gamma\lambda \text{TV}}(T^{k+1/2}) \\ O^{k+1} &= s_{\gamma\lambda\mu}(O^{k+1/2}). \end{cases}$$

**Algorithm 1:** Proposed method with Forward-Backward implementation in the Fourier domain.

the continuous TV as a Riemann summation over a grid at least two times finer than the critical sampling rate. In our case, instead of doubling the sampling rate, we choose to extend the spectral domain of  $T$  to an intermediate cell  $\mathcal{H}$ , in-between the *experimental frequency coverage*  $\mathcal{H}$ , and the cell  $\mathcal{C}$  corresponding to the (largely overcritical) spatial sampling rate of  $T$  (Figure 4).

There is another reason to use the *Spectral TV*. SMOS data

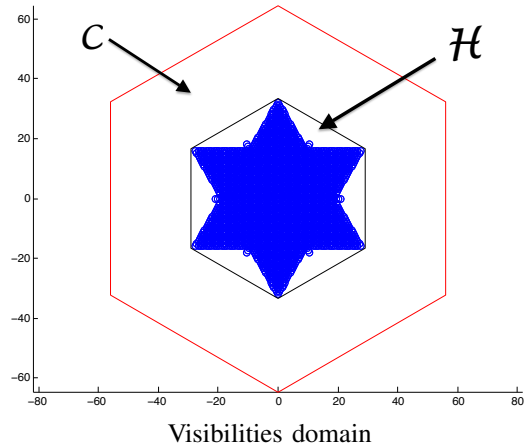


Fig. 4. Intermediate, hexagonally shaped cell  $\mathcal{H}$  used to reduce the staircasing effect inherent to discrete TV minimisation methods.

is captured on a hexagonal grid, and thus the variables  $T$  and  $O$  are modeled on a hexagonal grid as well. Most TV algorithms are based on the computation of derivatives using discrete differences, that are not straightforward to adapt to the hexagonal grid. This problem is avoided if we use the *Spectral TV*, because it computes the image derivatives analytically in the Fourier expansion. In what follows, we denote the *Spectral TV* of an image  $T$  based on the domain  $\mathcal{H}$  as  $\text{TV}_{\mathcal{H}}(T)$ .

#### IV. FINAL IMPLEMENTATION

##### A. Parameters choice

1) *Visibility noise estimation*: In the case of SMOS, the visibilities are always perturbed by a random radiometric noise, which is assumed to be uncorrelated (on the visibilities) and distributed according a Gaussian model with standard deviation [12]:

$$\sigma_{\Delta V_L} = \frac{T_A + T_R}{\sqrt{2B\tau}}, \quad (10)$$

where  $T_A$  is the antenna temperature,  $T_R$  is the receiver temperature,  $B$  is the bandwidth and  $\tau$  is the integration time. The bandwidth for MIRAS instrument is  $B = 19$  MHz and the integration time is  $\tau = 0.663$  seconds<sup>3</sup>. The other two variables ( $T_A$  and  $T_R$ ) depend on the observed scene and operational conditions. The value of those temperatures was reported to be  $T_A = 294$  K and  $T_R = 200$  K, leading to a noise standard deviation  $\sigma_{\Delta V_L} = 0.098$  K.

2) *Selection of  $\mu$* : Parameter  $\mu$  relates  $\text{TV}_{\mathcal{H}}(T)$  and  $S(O)$ . Depending on its value, a visual structure on the scene will be considered as an outlier (and therefore, assigned to the outliers image  $O$ ) or as part of the scene (the Earth *brightness temperature* image  $T$ ). Its value can be obtained as follows. Consider a cylinder  $c$  of radius  $r$  and height  $h$ . The involved norms or semi-norms are

$$\text{TV}(c) = 2\pi r h, \quad \|c\|_0 = \pi r^2 \mathbb{1}_{[h>0]}, \quad \|c\|_1 = \pi r^2 h.$$

When the sparsity operator is the  $\ell_1$  norm,  $c$  is considered as an outlier if  $\text{TV}(c) \geq \mu \|c\|_1$ , leading to  $\mu \leq \frac{2}{r}$ . In the examples, we have selected a value  $\mu \simeq \frac{2}{10} = 0.2$ , which amounts to consider that the radii of the outliers are at most 10 pixels wide. However, Earth structures spanning less than 10 pixels, can still be recovered by choosing a larger value for  $\mu$ .

In the case of the  $\ell_0$  norm, a cylinder is considered as an outlier as soon as  $\text{TV}(c) \geq \mu \|c\|_0$ , i.e.  $\mu \leq \frac{2h}{r}$ . Hence,  $\mu$  can then be interpreted as the minimal  $h/r$  outlier ratio. Here, contrarily to the  $\ell_1$  case, the height (here expressed in Kelvin units) plays an important role in distinguishing an outlier from the data, and larger values for  $\mu$  may be chosen ( $\mu \simeq 100 \frac{2}{10} = 20$ ).

3) *Selection of  $\lambda$* : Parameter  $\lambda$  has to be set carefully in order to make the unconstrained problem equivalent to the constrained one. A wrong value may drastically affect the results. The correct value of  $\lambda$  depends of course on  $|H|\sigma_{\Delta V_L}^2$ , which is given. A classical way to set  $\lambda$  programmatically is to use Uzawa's algorithm [23], described on Algorithm 2. Basically, the procedure consists in starting with a fixed  $\lambda^0$ , then solving the original problem with this  $\lambda^0$  and adjusting  $\lambda^k$  iteratively, depending on how near or how far the solution is to the original constraint. The procedure continues with ensured convergence until the data fit term is close enough to the expected noise  $|H|\sigma_{\Delta V_L}^2$ .

<sup>3</sup>Integration time is in fact 1.2 seconds, but it is adjusted by a factor of 1.81 to take into account correlation and sampling effects.

##### Uzawa

**input** : L1A SMOS Data - Visibilities:  $\tilde{V}$

**input** : Uzawa tolerance step:  $u_{tol}$

**output**: A temperature image  $T$ , an outliers image  $O$

**initialization**:

**Step 0**: Set  $T^0 = 0$  and  $O^0 = 0$ . Set  $\lambda^0$  with any suitable value ( for instance, 1).

**while**  $u_s > u_{tol}$  **do**

$(T^{k+1}, O^{k+1}) =$

$\min_{T,O} \|\mathbf{G}(T + O) - \tilde{V}\|_2^2 + \lambda^k (\text{TV}(T) + \mu S(O));$

$\lambda^{k+1} = \max\{\lambda^k + \rho \|\mathbf{G}(T^{k+1} + O^{k+1}) - \tilde{V}\|_2^2, 0\};$

$u_s = |\rho| \|\mathbf{G}(T^k + O^k) - \tilde{V}\|_2^2 - \sigma_{\Delta V_L}^2;$

**end**

**Algorithm 2:** Uzawa general algorithm applied to find the correct value  $\lambda$  that is consistent with  $|H|\sigma_{\Delta V_L}^2$  in the corresponding constrained minimization problem. Parameter  $\rho$  is set once for all to control the convergence rate. See [23] for further details.

##### B. Numerical optimization

Several methods have been proposed to accelerate the FB convergence rate. Two related approaches are FISTA [24] and monotone-FISTA [25]. The main difference between both methods and the FB algorithm is a clever combination of the two previous iterations, that increases the convergence rate. FISTA algorithm does not ensure monotone convergence (neither do FB), which is not a desirable property for an optimization algorithm. In [25], the authors introduce a monotone version of this algorithm known as MFISTA, that does not change the convergence rate of the original FISTA algorithm, but guarantees monotonicity. The final and complete algorithm is presented in Algorithm 3 but can be summarized as follows. It consists of two loops: an external loop that implements the *Uzawa* algorithm, solving the problem of finding the correct Lagrange multiplier  $\lambda$ . The internal loop implements de MFISTA algorithm, which is basically the FB algorithm with additional auxiliary variables to accelerate the convergence rate.

**About computational cost:** The number of iterations and convergence rate depend on each particular input data: if no RFIs are present in the image, the method converges much faster than the case of data with RFIs. The general process is slow: in data with RFIs it takes about 15,000 iterations, corresponding to several minutes (this is the case for instance in all the experiments with real data presented in the next section).

#### V. EXPERIMENTAL RESULTS

In this section we present results obtained on both simulated and real data. In both cases, we compare our approach to the nominal reconstruction process: the zero-padding approach [6] and the Blackman apodization approach [2].

### FINAL PROPOSED ALGORITHM

**input** : L1A SMOS Data - Visibilities:  $\tilde{V}$   
**input** : Uzawa tolerance step:  $\tau_u$   
**input** : MFista tolerance step:  $\tau_m$   
**output**: A brightness temperatures image  $T$ , an RFI image  $O$

**initialisation**: Set  $T^0 = 0$  and  $O^0 = 0$  ;  
**Initialize Uzawa**: Set  $\lambda^0 = 1$  and  $\rho \in (0..1]$  ;  
**while**  $e_u > \tau_u$  **do**  
  **Initialize MFISTA**: Set  $t^0 = 1$  and  $e_m > \tau_m$  ;  
  **while**  $e_m > \tau_m$  **do**  
     $(T_z^k, O_z^k) = \text{prox}_{\frac{\gamma}{L} E_2}(T^k, O^k) - \frac{\gamma}{L} \nabla E_1(T^k, O^k)$   
     $t^{k+1} = \frac{1 + \sqrt{1 + 4(t^k)^2}}{2}$   
     $(T_x^k, O_x^k) =$   
     $\arg \min_{(t,o) = \{(T_z^k, O_z^k), (T_x^{k-1}, O_x^{k-1})\}} E(t, o)$   
     $(T^{k+1}, O^{k+1}) =$   
     $(T_x^k + \frac{t^k - 1}{t^{k+1}}(T_z^k - T_x^{k-1}), O_x^k + \frac{t^k - 1}{t^{k+1}}(O_z^k - O_x^{k-1}))$   
    ;  
     $e_m = |E(T^{k+1}, O^{k+1}) - E(T^k, O^k)|$   
  **end**  
   $e_u = ||\mathbf{G}(T^k + O^k) - \tilde{V}||_2^2 - \sigma_{\Delta V_L}^2$  ;  
   $\lambda^{k+1} = \max\{\lambda^k + \rho ||\mathbf{G}(T^k + O^k) - \tilde{V}||_2^2, 0\}$   
**end**

**Algorithm 3:** Final proposed algorithm

#### A. Simulated Data

In order to have an overall idea of the proposed method's performance, we analyze it on different contexts:

- No RFIs are present in the image: only instrumental noise;
- RFIs with intensities in the same range as the Earth's brightness temperature plus instrumental noise;
- RFIs with intensities on a larger range ( $(0, 35000]$  K)<sup>4</sup> plus instrumental noise;
- RFIs located outside the image grid (with sub-pixel accuracy in non-integer positions) plus instrumental noise;
- Only the synthetic Earth's brightness temperature is considered (no instrumental noise or RFIs). This scenario is considered to evaluate the extrapolation power of the proposed approach.

The process to generate the simulated images is the following:

- 1) We generate a *brightness temperatures* image  $T_{gt}$ , based on [26], where *gt* stands for *ground truth*;
- 2) We obtain the visibilities associated to image  $T_{gt}$ :  $V_{gt} = \mathbf{G}T_{gt}$ ;
- 3) We generate a visibility noise random vector  $n$ , with independent identically distributed Gaussian entries with zero mean and covariance matrix  $\sigma_{\Delta V_L}^2 \mathbf{Id}$ ;
- 4) We add the noise visibilities to the ground truth visibilities to obtain an outlier-free noisy visibility vector:  $V = V_{gt} + n$ ;

<sup>4</sup>This range corresponds to the range we have observed on real data

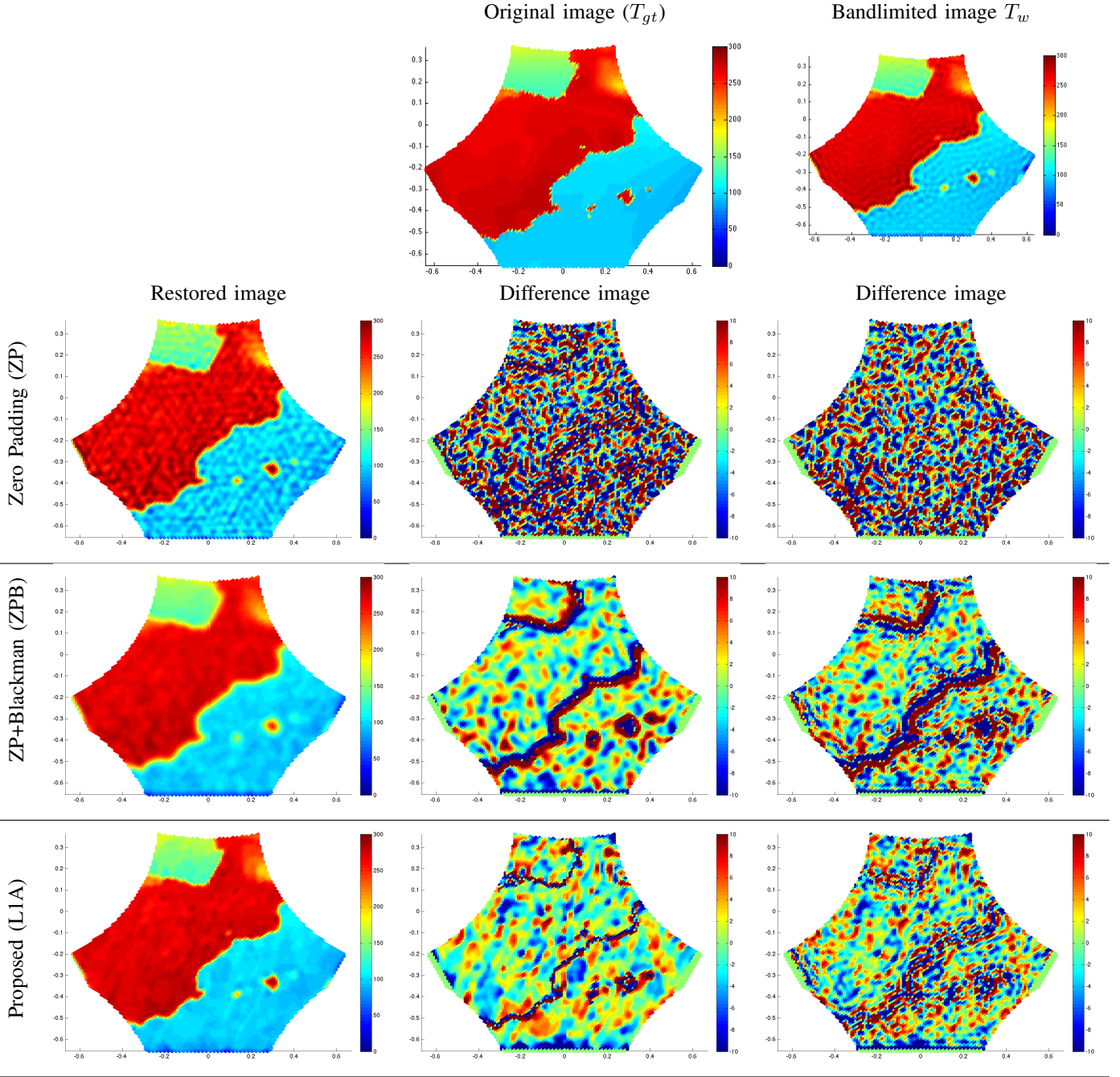
- 5) We generate a set of RFIs' images, one for each of the cases described above (no RFIs, RFIs in the image range, RFIs between  $(0, 35000]$  K and RFIs outside the grid positions). If we note  $T_\delta$  any of these synthetic RFIs' images, its corresponding induced visibilities is:  $V_\delta = \mathbf{G}T_\delta$ ;
- 6) Finally, we obtain the simulated visibilities adding both terms:  $V_f = V + V_\delta = V_{gt} + V_\delta + n$ , which are in full agreement with the image formation model.

The RFIs positions and intensity values are generated randomly, and the number of outliers varies from 2 to  $10^5$ .

**Error measurement:** In order to obtain a quantitative analysis the results, we need to define an error measure. Following [6], we consider the computation of the RMS error between the original image  $T$  and the recovered image  $T_r$ , over the entire Extended Alias-Free Field of View (E-AF-FOV). Because of the bandlimited property of the MIRAS instrument, even in an ideal case with no instrumental noise, we could not restore the original image  $T$ : only a smoothed version of  $T$  can be recovered. In [6], results are compared against a smoothed version of  $T$ , obtained by an inverse Fourier Transformation considering only the coefficients inside the *experimental frequency coverage*, denoted by  $T_w$ . Because we want to analyze the extrapolation properties of the presented method, we report the RMS error using both  $T_w$  and  $T$ : the RMS error computed against  $T_w$  describes the recovering capabilities of our method without considering the spectral extrapolation contribution, while the RMS error computed against  $T$  provides also this information.

Figure 5 shows the result of our method when applied to an image with no RFIs, but with instrumental noise. We recall that no modification to the functional is needed: we still consider the sparsity operator on an image  $O$ , whose values at the end of the minimization are all zero. Although the RMSE against the bandlimited image  $T_w$  is more or less the same for all methods, it is clear the improvement of the presented method when we look at the RMSE error computed against the original image  $T$ . This is a clear improvement, due mainly to the spectral extrapolation, that can also be seen on the edges of the difference images. This experiment confirms that the proposed method is generic, in the sense that it can be applied to images without RFIs. It is important to note one of the major drawbacks of the present method: small zones are removed. For instance Ibiza and Formentera islands are completely removed and Menorca is smoothed. This is also observed if we look the maximum error associated to each method: our method has the biggest value, which indicates that some structure was lost during restoration. This is expected by the value we set for  $\mu$ : any structure whose size is bigger than 10 pixels is considered an outlier. This value can be adjusted to obtain results that preserves smaller structures. Localization accuracy of RFIs can also be further improved by increasing the spatial resolution of our algorithm or by switching to a continuous outlier model as discussed in Section VI.

<sup>5</sup>This is not a limitation: it is based on the observation that rarely a real image has more than 10 outliers.



	RMSE( $T_{gt}$ )	Max Error( $T_{gt}$ )	RMSE( $T_w$ )	Max Error( $T_w$ )
$T_{ZP}$	13.160	108.523	8.936	37.513
$T_{ZPB}$	13.612	143.147	9.933	70.018
$T_{L1A}$	9.2245	145.523	6.661	44.366

Fig. 5. Comparison with previous approaches when no outliers are present in the image. Error measures are expressed in Kelvin units and the error range on the images is set between  $[-10,10]$  K. For this experiment, parameter  $\mu$  was set to 2.0 (corresponding to RFI of at least 1 pixel radius).  $T_{ZP}$ ,  $T_{ZPB}$  and  $T_{L1A}$  denotes the results obtained by the Zero Padding method, the Blackman apodization method, and the method proposed in this work respectively.



Figures 6 and 7 show the results obtained when RFIs are present in the scene. In the first case, the RFIs intensities fall within the Earth’s brightness temperature range; in the second case, the RFIs intensities range from 0 to 35000 K. Here again, the proposed method is consistently better than the zero padding approach and even in the presence of very large outliers (35000 K) the maximum error is 200 times smaller, leaving an error of near 150 K, which is in the order of the ground truth image values. In these examples the loss of small structures becomes more evident: all Balears islands were removed.

In Figure 8 we present the results obtained when the outliers are not located on the sampling grid points. It can be observed that the performance of the proposed method continues to be consistent with the case where the outliers were located on the grid.

Table I summarizes the quantitative measures corresponding to the results obtained with the proposed method in all the simulated scenarios. It is clear that the method behaves consistently in all of them. We can conclude that the method is well adapted for several contexts that may occur on real data, and that no context-dependent strategies are needed in order to apply it. In other words, the method and its parameters can be set once for all, independently on the observed data.

We end this set of experiments on synthetic data with an analysis of the spectral extrapolation capability of the proposed method. In this test, we only analyse the results of the bandpass effect of the MIRAS instrument. No instrumental noise or outliers are added to the input ground truth image. For this experiment, the outliers’ support in the proposed model was set to 1 pixel, following the strategy described in Section IV-A2. Results are displayed on Figure 9. In the first row, we show the result of computing  $T_{LIB} = \mathbf{J}^+ \mathbf{G} T_{gt}$ . The error reported on the corresponding table is only related to the bandpass matrix  $\mathbf{G}$  and zero padding solution with its corresponding matrix  $\mathbf{J}^+$ . It is clear from this example that our method truly performs a spectral extrapolation, whose effects can be easily observed both on the image edges and on the reduction of Gibbs oscillations in the hole image. These two aspects can also be observed in the associated table, on the reported values of RMSE against the original image  $T$  and the bandlimited version  $T_w$ . It is clear that the zero-padding approach is better to obtain the bandlimited version of the image: the RMSE is only 0.55, against 5.10 for the proposed method. Nevertheless, when we compare against the original  $T$  image, the result obtained using the proposed method is consistently better: the RMSE is 7.86 (against 9.67 for the zero-padding method), the maximum error is much lower and also the difference image presents much less structure than on the zero-padding approach. One final remark: note that in this case, when parameter  $\mu$  is set considering an outlier of 1 pixel radius, the small structures are kept (observe the presence of all Balears islands). This suggests that, when no RFIs are present in the image, we can set much larger value for  $\mu$ , leading to better results.

## B. Experiments on real data

The second set of experiments was performed on real data. Experiments were performed on several snapshots and datasets. Here, for the sake of brevity, we illustrate typical results presenting two snapshots taken on march 2010. We have set  $\sigma_n$  equal to 0.1, which is the measurement error reported by the SMOS mission. Figures 10 and 11 show the results obtained for snapshots 996 and 1050, that correspond to central Europe (Italy) and Northern Europe (Denmark and England) respectively.

Note that the acquired images are corrupted by several outliers that considerably degrade the data. It is clear that the proposed approach outperforms both the Zero Padding approach and the corresponding Blackman apodization method. An effect that can be seen, in particular in the L1A-based restored brightness temperature image of central Europe, is the correlation between land humidity and topography. Note, for instance, the consistency of the humidity flow coming from the Adriatic Sea and entering inlands in northern Italy, stopped by the barrier imposed by the Alps.

## VI. CONCLUSIONS AND FUTURE WORK

In this work we propose a novel approach for the restoration of images acquired by the SMOS mission. Two fundamental contributions are presented: First, a variational approach that seeks to restore the image of the Earth’s brightness temperature on one side, and the image of outliers or RFIs on the other side. The second contribution is the use of the visibilities or L1A data product directly for the restoration of corrupted images with RFIs, when most of the previous work use the temperatures obtained by zero padding regularisation as input (L1B data product).

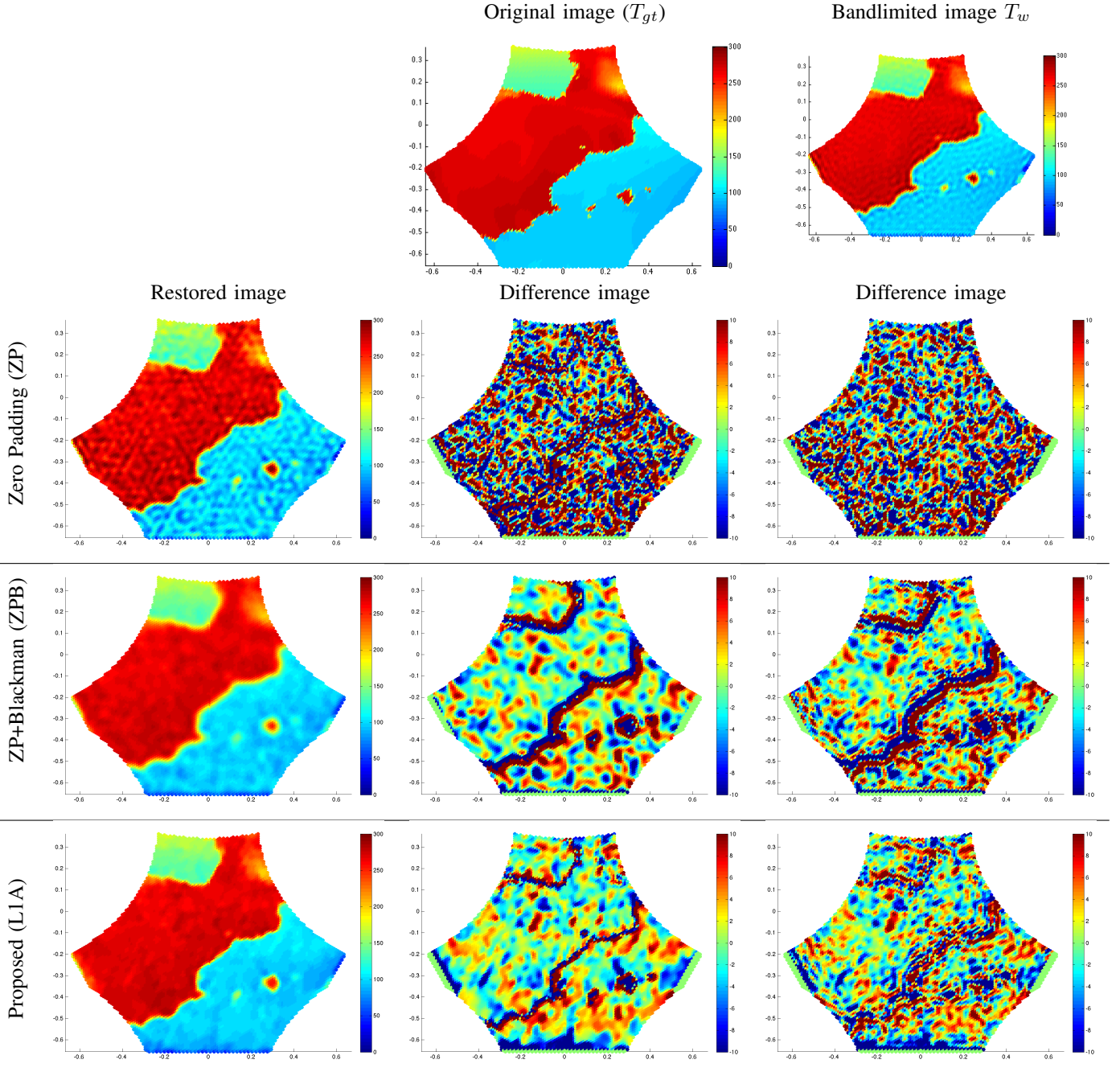
The parameters in the model are fixed once for all or automatically adjusted by the optimization procedure, since they are either derived from physical modeling or obtained by formal procedures. Experiments on synthetic data show the ability of our method to recover the Earth’s brightness temperature with high precision.

In summary, experiments both on synthetic and real data confirm the suitability of the proposed method, and show that results are of very high quality, outperforming previous approaches proposed for SMOS images restoration. On the other hand, the drawback of the proposed method is the time it requires to restore each snapshots (several minutes). However, this could be dramatically reduced using parallelization strategies.

## APPENDIX PROXIMAL OPERATORS

For the sake of completeness, we include the derivation of each of the proximal operators involved in this work. We first recall the proximal operator definition of a functional  $E$ :

$$\text{prox}_{\gamma E}(x) = \arg \inf_y E(y) + \frac{1}{2\gamma} \|x - y\|^2.$$



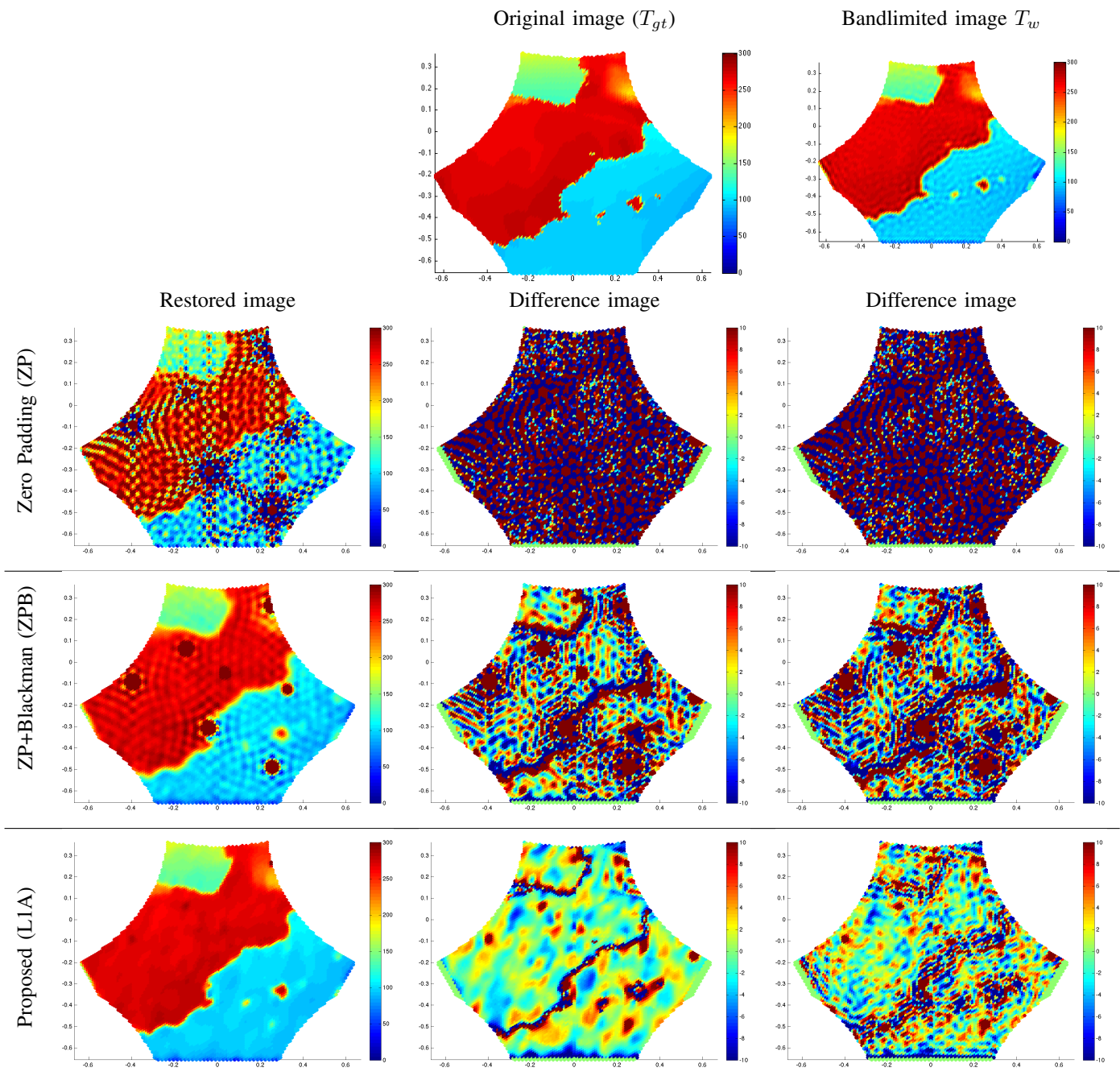
	RMSE( $T_{gt}$ )	Max Error( $T_{gt}$ )	RMSE( $T_w$ )	Max Error( $T_w$ )
$T_{ZP}$	13.733980	101.325733	9.787204	63.695435
$T_{ZPB}$	13.726109	140.964082	10.078270	69.381071
$T_{L1A}$	10.416675	147.356192	9.454039	112.115255

Fig. 6. Analysis of the different methods when the outliers intensities fall within the range of the Earth's brightness temperatures. Error measures are expressed in Kelvin.  $T_{ZP}$ ,  $T_{ZPB}$  and  $T_{L1A}$  denotes the results obtained by the Zero Padding method, the Blackman apodization method, and the method proposed in this work respectively.

	RMSE( $T_{gt}$ )	Max Error( $T_{gt}$ )	RMSE( $T_w$ )	Max Error( $T_w$ )
No outliers present in the image	10.743735	142.671738	7.644904	75.479853
Outliers with values on the image range	10.416675	147.356192	7.266313	57.133400
Outliers in the range [0,35000] K	13.082794	170.410338	10.678159	149.955697
Outliers outside grid position (25000 K)	11.945941	166.184179	9.403918	133.394016

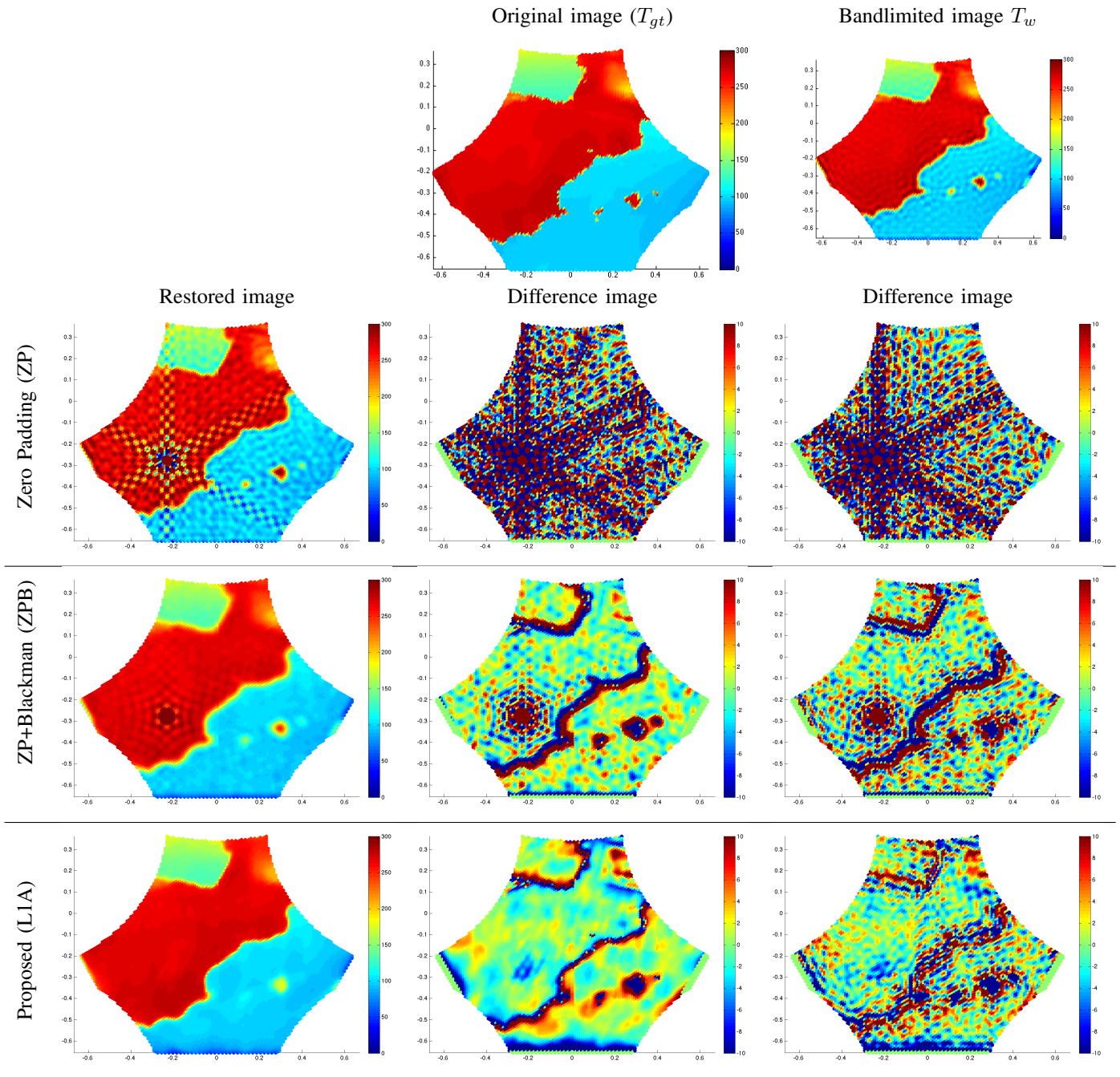
TABLE I

QUANTITATIVE RESULTS OBTAINED WITH THE PROPOSED METHOD FROM SIMULATED DATA, IN DIFFERENT SCENARIOS: WITHOUT OUTLIERS, WITH OUTLIERS INTENSITIES WITHIN THE RANGE OF THE IMAGE, WITH OUTLIERS LOCATED ON THE SAMPLING GRID POSITIONS AND OUTSIDE OF IT.



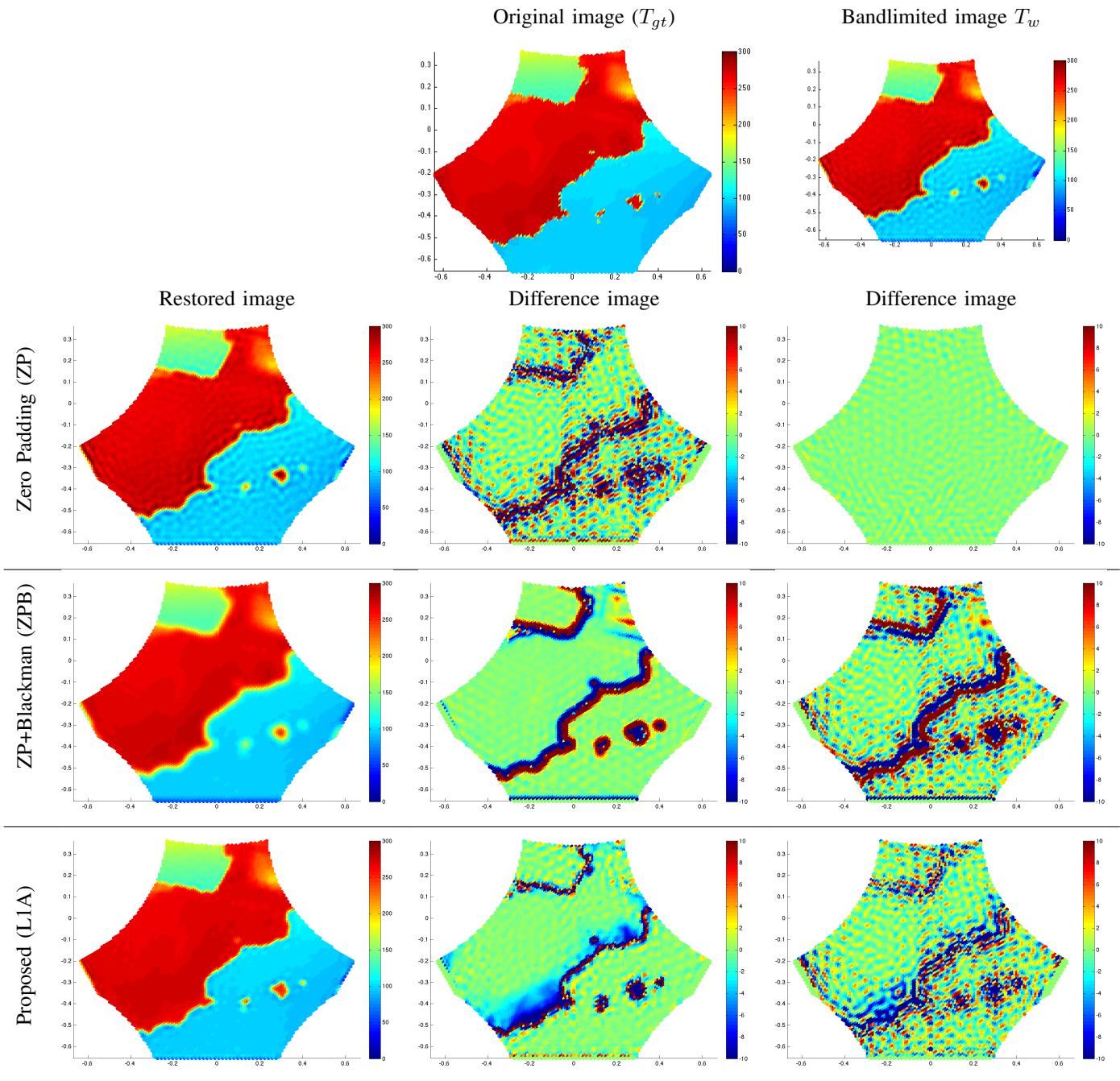
	RMSE( $T_{gt}$ )	Max Error( $T_{gt}$ )	RMSE( $T_w$ )	Max Error( $T_w$ )
$T_{ZP}$	248.437399	5985.546374	248.253076	5988.876063
$T_{ZPB}$	112.882746	2132.461092	112.498513	2135.790782
$T_{L1A}$	13.082794	170.410338	10.678159	149.955697

Fig. 7. Results obtained with simulated data when several outliers with different intensities are present on the image. In this example, outliers are generated on the following grid positions with its corresponding values:  $(-0.0357, -0.3093)$ , 35.000 K;  $(-0.1429, 0.0619)$ , 10000 K;  $(-0.3929, -0.0928)$ , 25000 K;  $(0.5714, -0.1753)$ , 800 K;  $(0.3304, -0.1289)$ , 8000 K;  $(0.2589, 0.2629)$ , 35000 K;  $(0.2589, -0.4897)$ , 30000 K;  $(0.0357, -0.0515)$ , 2000 K (Recall that this information is not used during the restoration process: it is only provided for a better understanding of the Figure.). Error measures are expressed in Kelvin units and the error range on the images is set between  $[-10, 10]$  K.  $T_{ZP}$ ,  $T_{ZPB}$  and  $T_{L1A}$  denotes the results obtained by the Zero Padding method, the Blackman apodization method, and the method proposed in this work respectively.



	RMSE( $T_{gt}$ )	Max Error( $T_{gt}$ )	RMSE( $T_w$ )	Max Error( $T_w$ )
$T_{ZP}$	87.283054	3335.698589	86.752718	3336.383413
$T_{ZPB}$	41.005901	1185.824560	39.933994	1186.509384
$T_{L1A}$	11.945941	166.184179	9.403918	133.394016

Fig. 8. Analysis of the different methods when the the outliers are not located on the sampling grid. Note that the method performs well, with a performance similar to the one obtained when outliers are present on grid positions. In this experiment, the outlier introduced in the image has an intensity of 20000 K. Error measures are expressed in Kelvin units and the error range on the images is set between  $[-10,10]$  K.  $T_{ZP}$ ,  $T_{ZPB}$  and  $T_{L1A}$  denotes the results obtained by the Zero Padding method, the Blackman appodization method, and the method proposed in this work respectively.



	RMSE( $T_{gt}$ )	Max Error( $T_{gt}$ )	RMSE( $T_w$ )	Max Error( $T_w$ )
$T_{ZP}$	9.671122	110.410052	0.557796	2.717416
$T_{ZPB}$	13.071849	144.637200	9.179310	63.214112
$T_{LIA}$	7.858867	89.453253	5.101420	54.833780

Fig. 9. Comparison of extrapolation results. Error measures are expressed in Kelvin units and the error range on the images is set between  $[-10,10]$  K.  $T_{ZP}$ ,  $T_{ZPB}$  and  $T_{LIA}$  denotes the results obtained by the Zero Padding method, the Blackman appodization method, and the method proposed in this work respectively. See text for details.

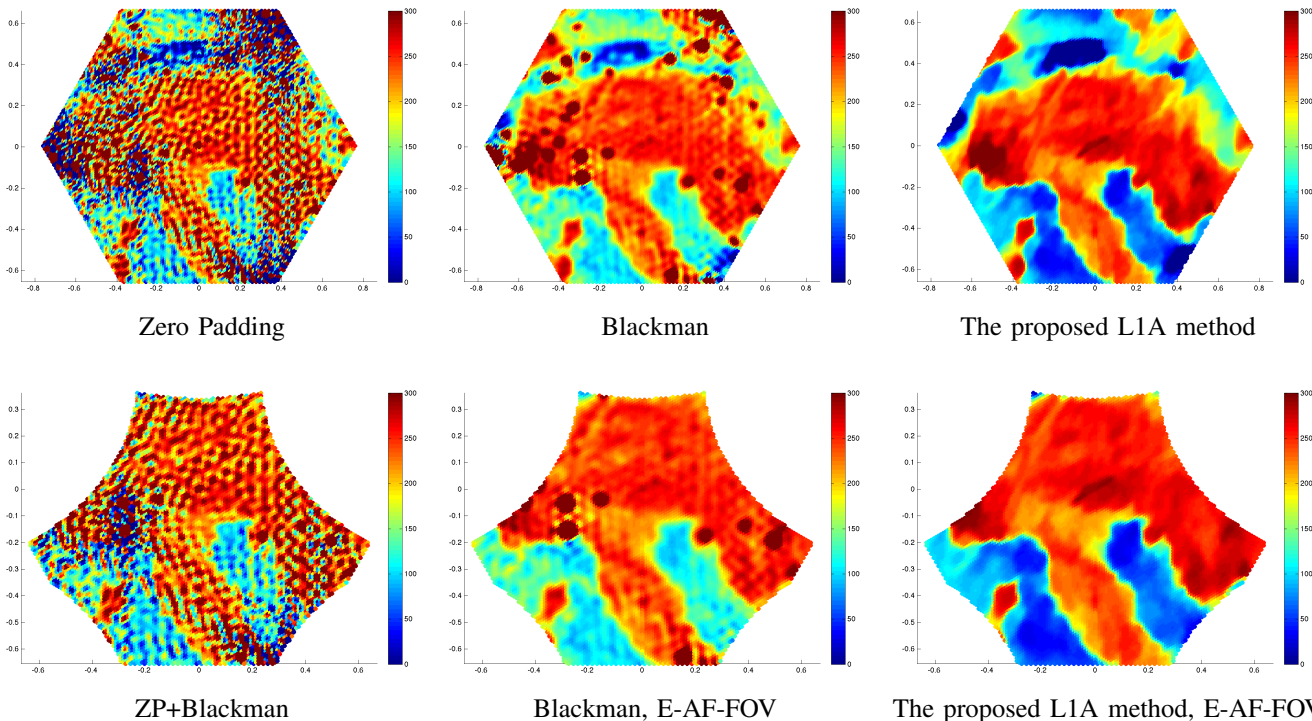


Fig. 10. Comparison between previous works and our method. This snapshot corresponds to Central Europe, with Italy clearly visible, and was acquired on march 2010. Color scale ranges from 0 to 300 Kelvin.

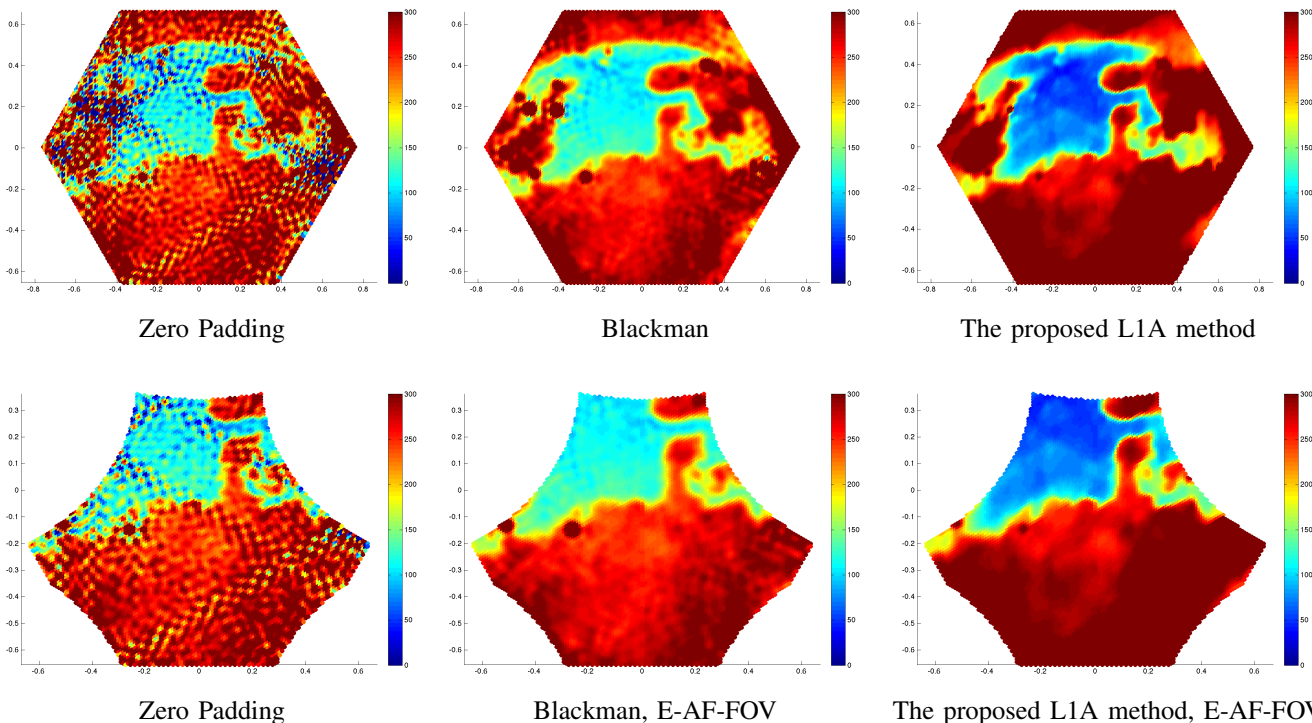


Fig. 11. Comparison between previous works and our method. This snapshot corresponds to Northern Europe and was acquired on march 2010. Color scale ranges from 0 to 350 Kelvin.

**Proposition 2** (Proximal operators of  $\ell_0$  and  $\ell_1$  norms),  $\text{prox}_{\gamma\|\cdot\|_1}(o)[i] = \tau_\gamma(o[i])$ ,  $\text{prox}_{\gamma\|\cdot\|_0}(o)[i] = s_\gamma(o[i])$ , where

$$\tau_\gamma(t) = \begin{cases} \text{sign}(t)(|t| - \gamma) & \text{if } |t| \geq \gamma \\ 0 & \text{if } |t| < \gamma \end{cases}$$

$$s_\gamma(t) = \begin{cases} |t| & \text{if } |t| \geq \gamma \\ 0 & \text{if } |t| < \gamma \end{cases}$$

are the hard and soft thresholding operators, respectively.

#### A. Derivation of the proximal operator of $\text{TV}_{\mathcal{H}}$

We recall first the definition of the total variation semi-norm of an image  $u : \Omega \subset \mathbb{R}^2 \rightarrow \mathbb{R}$ :

$$\text{TV}(T) = \sup_{\psi \in C^1(\Omega, \mathbb{R}^2), \|\psi\|_{L^\infty(\Omega)} \leq 1} \left\{ \int_{\Omega} u(x) \text{div } \psi(x) dx \right\},$$

where  $C^1(\Omega, \mathbb{R}^2)$  denotes the space of continuously differentiable functions of compact support contained in  $\Omega$ . With this notation,  $\text{prox}_{\gamma\text{TV}}$  can be expressed:

$$\text{prox}_{\gamma\text{TV}}(u) = \arg \inf_y \text{TV}(y) + \frac{1}{2\gamma} \|u - y\|^2.$$

Chambolle [15] proves that the solution to this minimization problem can be expressed as the projection into a suitable convex set:

**Proposition 3.** *The unique solution for  $\text{prox}_{\gamma\text{TV}}(u)$  is given by  $y = u - P_{\gamma G}(y)$ , where  $P_{\gamma G}(y)$  is the projection of  $y$  into the set  $\gamma G$ , and  $G = \{v \in X; \exists p \in X, |p| \leq 1 \text{ s.t. } v = \text{div } p\}$ . The set  $X = \mathbb{R}^{N^2}$  is the set of all discrete images of size  $N^2$ .*

The projection  $P_{\gamma G}(y)$ , defined by

$$\arg \min_{p \in X \times X, |p_{i,j}| \leq 1 \forall i,j=1,\dots,N} \{ |\gamma \text{div } p - u|_{X \times X}^2 \},$$

can be computed iteratively as

$$p_{i,j}^{n+1} = \frac{p_{i,j}^n + \tau(\nabla(\text{div } p^n - u/\gamma))_{i,j}}{1 + \tau|\nabla(\text{div } p^n - u/\gamma))_{i,j}|}.$$

Chambolle [15] has proven that, if  $0 < \tau \leq \frac{1}{8}$  then  $\gamma \text{div } p^n$  converges to  $P_{\gamma G}(y)$  as  $n \rightarrow \infty$ . Finally,

$$\text{prox}_{\gamma\text{TV}}(u) = u - \lim_{n \rightarrow \infty} \gamma \text{div } p^n.$$

In our case, the spectral TV minimization consists in restricting the frequency domain to the cell  $\mathcal{H}$ , *i.e.*

$$\min_{u \in \text{BL}(\mathcal{H})} \text{TV}(u) + \text{DataFit}(u),$$

where  $\text{BL}(\mathcal{H})$  denotes the space of band limited functions with spectral support within  $\mathcal{H}$ . This constraint can be integrated into the TV operator by means of the indicator function:

$$\iota_A(x) = \begin{cases} 0 & \text{if } x \in A \\ +\infty & \text{if } x \notin A \end{cases}$$

Then the proximal operator for the spectral TV becomes

$$\text{prox}_{\gamma\text{TV}_{\mathcal{H}}}(u) := \text{prox}_{\gamma\text{TV} + \iota_{\text{BL}(\mathcal{H})}}(u).$$

Since the sub differential of the indicator function  $\iota_A$  is the projection operator  $P_A$ , we can easily show from the previous

expression that a slight modification in Chambolle's algorithm yields the proximal operator for the spectral TV:

**Proposition 4.** *Let  $u \in \text{BL}(\mathcal{H})$ , and  $0 < \tau \leq \frac{1}{8}$ . Then the following algorithm with  $u^n = -\gamma v^n$  converges to  $\text{prox}_{\gamma\text{TV}_{\mathcal{H}}}(u)$*

- 1)  $p^0 = 0$ ,  $v^0 = -u/\gamma$ ,  $n = 0$
- 2)  $p^{n+1} = P_{\text{BL}(\mathcal{H})} \left( \frac{p^n + \tau \nabla v^n}{1 + \tau \|\nabla v^n\|} \right)$
- 3)  $v^{n+1} = \text{div } p^n + v^0$
- 4) *If not converged go to step 2*

Note that the only modification with respect to Chambolle's algorithm is the spectral projection  $P_{\text{BL}(\mathcal{H})}$  at each iteration  $p^n$ .

#### REFERENCES

- [1] Y. Kerr, P. Waldteufel, J.-P. Wigneron, S. Delwart, F. Cabot, J. Boutin, M.-J. Escorihuela, J. Font, N. Reul, C. Gruhier, S. Juglea, M. Drinkwater, A. Hahne, M. Martin-Neira, and S. Mecklenburg, "The SMOS mission: New tool for monitoring key elements of the global water cycle," *Proceedings of the IEEE*, vol. 98, no. 5, pp. 666–687, May 2010.
- [2] K. D. McMullan, M. Brown, M. Martin-Neira, W. Rits, S. Ekholm, J. Marti, and J. Lemanczyk, "SMOS: The payload," *Geoscience and Remote Sensing, IEEE Transactions on*, vol. 46, no. 3, pp. 594–605, March 2008.
- [3] M. Martin-Neira, Y. Menard, J. Goutoule, and U. Kraft, "MIRAS, a two-dimensional aperture synthesis radiometer," in *IEEE International Geoscience and Remote Sensing Symposium 1994. Surface and Atmospheric Remote Sensing: Technologies, Data Analysis and Interpretation*, vol. 3, Aug 1994, pp. 1323–1325.
- [4] Y. Kerr, J. Font, P. Waldteufel, A. Camps, J. Bara, I. Corbella, F. Torres, N. Duffo, M. Vallillossera, and G. Caudal, "New radiometers: SMOS - a dual pol L-band 2D aperture synthesis radiometer," in *Aerospace Conference Proceedings, 2000 IEEE*, vol. 5, 2000, pp. 119–128.
- [5] I. Corbella, N. Duffo, M. Vall-llossera, A. Camps, and F. Torres, "The visibility function in interferometric aperture synthesis radiometry," *IEEE Trans. Geosci. Remote Sensing*, vol. 42, no. 8, pp. 1677–1682, 2004.
- [6] E. Anterrieu, "A resolving matrix approach for synthetic aperture imaging radiometers," *IEEE Transactions on Geoscience and Remote Sensing*, vol. 42, no. 8, pp. 1649–1656, Aug 2004.
- [7] D. Petersen and D. Middleton, "Sampling and reconstruction of wave-number-limited functions in N-dimensional euclidean space," *Information and Control*, vol. 5, pp. 279–323, 1962.
- [8] A. Camps, J. Bara, I. Sanahuja, and F. Torres, "The processing of hexagonally sampled signals with standard rectangular techniques: application to 2-D large aperture synthesis interferometric radiometers," *IEEE Transactions on Geoscience and Remote Sensing*, vol. 35, no. 1, pp. 183–190, Jan 1997.
- [9] A. R. Thompson, J. M. Moran, and G. W. Swenson, *Interferometry and Synthesis in Radio Astronomy; 2nd ed.* Weinheim: Wiley-VCH, 2001.
- [10] A. Camps, M. Vall-llossera, I. Corbella, N. Duffo, and F. Torres, "Improved image reconstruction algorithms for aperture synthesis radiometers," *Geoscience and Remote Sensing, IEEE Transactions on*, vol. 46, no. 1, pp. 146–158, Jan 2008.
- [11] J. Preciozzi, P. Musé, A. Almansa, S. Durand, A. Khazaal, and B. Rougé, "SMOS images restoration: A sparsity-based variational approach," in *IEEE International Geoscience and Remote Sensing Symposium*, 2014.
- [12] C. S. Ruf, C. T. Swift, A. B. Tanner, and D. M. Le Vine, "Interferometric synthetic aperture microwave radiometry for the remote sensing of the earth," *Geoscience and Remote Sensing, IEEE Transactions on*, vol. 26, no. 5, pp. 597–611, 1988.
- [13] F. Malgouyres and F. Guichard, "Edge direction preserving image zooming: a mathematical and numerical analysis," *SIAM Journal on Numerical Analysis*, vol. 39, no. 1, pp. 1–37, 2001.
- [14] M. Elad, *Sparse and Redundant Representations: From Theory to Applications in Signal and Image Processing.* Springer, 2010.
- [15] A. Chambolle, "An algorithm for total variation minimization and application," *Journal of Mathematical Imaging and Vision*, vol. 20, no. 1, 2004.
- [16] A. Chambolle and T. Pock, "A first-order primal-dual algorithm for convex problems with applications to imaging," *Journal of Mathematical Imaging and Vision*, vol. 40, no. 1, pp. 120–145, 2011.

- [17] P. L. Combettes and V. R. Wajs, "Signal recovery by proximal forward-backward splitting," *SIAM Journal on Multiscale Modeling and Simulation*, vol. 4, no. 4, pp. 1168–1200, 2005.
- [18] T. Blumensath and M. E. Davies, "Iterative thresholding for sparse approximations," *The Journal of Fourier Analysis and Applications*, vol. 62, pp. 291–294, January 2008.
- [19] E. Anterrieu, P. Waldteufel, and A. Lannes, "Apodization functions for 2-D hexagonally sampled synthetic aperture imaging radiometers," *IEEE Transactions on Geoscience and Remote Sensing*, vol. 40, no. 12, pp. 2531–2542, Dec 2002.
- [20] M. Nikolova, "Local strong homogeneity of a regularized estimator," *SIAM Journal on Applied Mathematics*, vol. 61, no. 2, pp. 633–658, 2000.
- [21] K. Jalalzai, "Some remarks on the staircasing phenomenon in total-variation based image denoising," *ArXiv e-prints*, Feb. 2014.
- [22] L. Moisan, "How to discretize the total variation of an image?" *ICIAM07 Minisymposia*, 2007.
- [23] H. Uzawa, "Iterative methods for concave programming," *Studies in linear and nonlinear programming*, vol. 6, 1958.
- [24] A. Beck and M. Teboulle, "A fast iterative shrinkage-thresholding algorithm for linear inverse problems," *SIAM Journal on Imaging Sciences*, vol. 2, no. 1, pp. 183–202, 2009.
- [25] ———, "Fast gradient-based algorithms for constrained total variation image denoising and deblurring problems," *IEEE Transactions on Image Processing*, vol. 18, no. 11, pp. 2419–2434, 2009.
- [26] A. Camps, I. Corbella, M. Vall-llossera, N. Duffo, F. Marcos, F. Martínez-Fadrique, and M. Greiner, "The SMOS end-to-end performance simulator: Description and scientific applications," in *IEEE International Geoscience and Remote Sensing Symposium*, vol. 1, 2003, pp. 13–15.